7th High Performance Yacht Design Conference
Auckland, 11-12 March 2021

ON THE EFFECT OF THE LEADING-EDGE SEPARATION BUBBLE ON THE AERODYNAMICS OF SPINNAKERS

Jean-Baptiste R. G. Souppez[1], j.souppez@aston.ac.uk
Patrick Bot[2], patrick.bot@ecole-navale.fr
Ignazio Maria Viola[3], i.m.viola@ed.ac.uk

Abstract. The spinnaker is the most powerful and one of the most used sails both in racing and cruising - yet its complex aerodynamics governed by flow separation is still not fully understood. While the flow around a spinnaker is unsteady and highly tridimensional, locally the governing fluid mechanics may be represented by the quasi-steady bidimensional flow around a cambered circular arc with a sharp leading edge. The spinnaker is typically trimmed such that the stagnation point is at the leading edge with the sail streamline separating on the suction side and reattaching within the first 10% of the chord length, forming a leading-edge separation bubble (LESB). This flow feature sets the beginning of the boundary layer, whose separation further downstream is paramount for the global aerodynamic forces on the sail. This study investigates the effect of the LESB on the boundary layer regime and downstream flow separation through particle image velocimetry on a circular arc. The existence of the combination of a critical Reynolds number and a critical angle of attack to trigger turbulent separation is demonstrated. A turbulent LESB followed by a laminar boundary layer is observed in sub-critical regime. Conversely, in a post-critical condition, a turbulent LESB ensued by a turbulent boundary layer is detected, the latter continuing all the way to trailing-edge separation. This behaviour ultimately yields a sharp lift increase and drag reduction. These findings reveal the critical effect of the leading-edge vortical structures on the global flow field and forces experienced by cambered wings with leading-edge separation, including high performance spinnakers. It is envisaged that these results will contribute to improve the design and performance of downwind yacht sails.

1. NOMENCLATURE

AR	Aspect ratio (s/c)
c	Chord length (m)
C_D	Drag coefficient
C_L	Lift coefficient
D	Drag (N)
f	Chordwise maximum draft location (m)
L	Lift (N)
Re	Reynolds number
s	Span (m)
t	Thickness (m)
u	Streamwise flow velocity (m.s^{-1})
u'	Streamwise flow velocity fluctuation (m.s^{-1})
U_∞	Freestream flow velocity (m.s^{-1})
v'	Streamnormal velocity fluctuation (m.s^{-1})
x	Streamwise coordinate (m)
x_s	Streamwise position of the separation point (m)
y	Streamnormal coordinate (m)
y_c	Sail camber (m)
α	Angle of attack (°)
Γ	Circulation (m^2.s^{-1})
κ	Nondimensional turbulent kinetic energy
ρ	Fluid density (kg.m^{-3})
LESB	Leading-edge separation bubble
PIV	Particle image velocimetry
RANS	Reynolds-averaged Navier-Stokes
TKE	Turbulent kinetic energy

2. INTRODUCTION

Modern symmetric spinnakers appeared in the 1960s and further developed in the 1970s, before asymmetric spinnakers were introduced in the 1980s in the 18ft fleet in Sydney, and then popularised on offshore racing yachts in the 1990s. These new sails were promptly adopted in many prominent sailing events, from offshore races to the America's Cup [1, 2, 3]. Indeed, the 1995 edition of the America's Cup gave greater importance to downwind legs [1], thus prompting further developments. Because of the complexity of the flow around downwind sails, the necessity to undertake experimental tests was perceived [4], ultimately resulting in dedicated experimental facilities, namely twisted flow wind tunnels [5]. On the other hand, the 1990s also coincide with a fast increase in accessible computational power, allowing advanced numerical methods [6]. As downwind sails feature a high camber and the flow is largely separated, the use of Reynolds-averaged Navier-Stokes (RANS) simulations is necessary [7], with the first instance of RANS models occurring in 1996 for spinnakers [8]. This is in contrast with upwind sails, exhibiting lower camber and largely attached flow. As a result, these have been successfully analysed using inviscid codes since the 1960s [9, 10], methods that have been extensively utilized in America's Cup sails development [11].

The flow around spinnakers is unsteady and highly tridimensional, owing to the complex 3D geometry of the sail. However, locally, the governing fluid mechanics may be represented by the quasi-steady bidimensional flow around a highly cambered, thin circular arc with a sharp leading edge [12, 13, 14].

[1] Senior Teaching Fellow, College of Engineering and Physical Sciences, Aston University, UK.
[2] Associate Professor, Naval Academy Research Institute, Brest, France.
[3] Reader, School of Engineering, Institute for Energy Systems, University of Edinburgh, UK.

Spinnakers are typically trimmed such that the stagnation point is at the leading edge with the sail streamline separating on the suction side and reattaching within the first 10% of the chord length, forming a leading-edge separation bubble (LESB), also referred to in the literature as a leading-edge bubble. This flow feature sets the beginning of the boundary layer, whose separation further downstream is paramount for the global aerodynamic forces on the sail.

This study investigates the effect of the LESB on the boundary layer regime and downstream flow separation through particle image velocimetry (PIV) on a circular arc. First, the literature inherent to low and high camber circular arcs is reviewed. Then, the experimental setup is presented, and subsequently validated to ensure flow bidimensionality and measurement accuracy. The results eventually present novel findings on the effect of the leading-edge separation bubble on the aerodynamics of modern asymmetric spinnakers, including the flow fields and global forces.

3. BACKGROUND ON CIRCULAR ARCS

3.1. Low camber ($y_c \leq 0.2c$) circular arcs

Early instances of experiments on circular arcs can be traced back to Wallis [15]. Later, tests on bent plates were undertaken by Maekawa & Atsumi [16], that refined the idea of a critical Reynolds number (Re) originally introduced by Tani [17], and eventually resulting in the definition of the O-K criterion [18]. A circular arc with a camber-to-chord ratio (y_c/c) of 7.5% was tested by DeLaurier & Harris [19] for an atypical application, namely paper model airplanes. The work of Buehring [20] on windmills, later expanded by Bruining [21] tackled a circular arc with y_c/c = 10%, while Pandey et al. [22] undertook wind tunnel testing of various circular arcs up to y_c/c = 14%.

Additional investigations into low camber circular arcs were performed by Tse [23], who tested 5%, 7.5% and 10% camber-to-chord ratios, subsequently complemented by Cyr [24], with the addition of an 18% thin cambered aerofoil with a sharp leading edge. A larger y_c/c = 20% was considered in Sunada et al. [25] as part of a parameter study, including camber-to-chord ratios of 5%, 10% and 20%. The results highlighted the drastic changes in behaviours with greater camber, such as increased lift and delayed stall, supported by the later findings of Okamoto & Azuma [26] on 3D circular arcs.

The geometries previously discussed had a thickness-to-chord ratio (t/c) circa 5%, i.e. similar to the experiments of Velychko [27], Flay et al. [12] and Bot [13], with a value close to 4%. These remain relatively high when compared to membranes or sails, and thus a smaller value should be targeted to achieve as thin a wing as possible while structurally suitable for experimental campaigns.

Furthermore, Sunada et al. [25] eventually concluded that a thin aerofoil with a sharp leading edge is paramount for performance, based on the comparison of force coefficients, and noted that performance is strongly affected by leading edge vortices. This implies that promoting the appearance of the leading-edge separation bubble with a thin and sharp leading edge improves performance. Moreover, Okamoto & Azuma [26] revealed that sharpening the leading edge does provide benefits analogous to those of a higher camber profile. Finally, the work of Brault [28] also supports these findings, demonstrating the benefits of a sharp leading edge over a chamfered one.

Consequently, it appears that only very few historical studies tackled y_c/c in excess of 20%, with further limitations in terms of both thickness and leading edge shape. While the original study of a 20% camber sail by Milgram [29] is worth mentioning, it is the recent literature on modern asymmetric downwind yacht sails that proves most relevant. Indeed, highly cambered (22% < y_c/c < 25%), thin circular arcs with a sharp leading edge were adopted as a 2D simplification of the more complex 3D shape of downwind sails. A greater focus on flow visualisation and flow features are also core elements of the newer literature, thereby extending beyond comparative force measurements.

3.2. High camber ($y_c > 0.2c$) circular arc for downwind sails application

The pressure distribution of membranes, equivalent to circular arc sails with high camber-to-chord ratios ranging from 19.3% to 25.7% was the focus of Cyr & Newman [30], thereby representing one of the earliest studies into higher camber. Although the exact Reynolds number or angle of attack (α) are not specified, the pressure distribution of a similar high camber arc was tested by Flay et al. [12], yielding a comparable qualitative behaviour.

Since 2006, highly cambered circular arcs have been extensively studied [12, 13, 14, 31, 32, 33, 34, 35]. Sharp transitions in lift forces were identified and related to variations in flow patterns, as summarized by Bot [13, 36] while additional correlation between forces and flow fields were provided by Souppez et al. [14, 37].

From the published experimental results of Bot [13], depicted in Figure 1, it is possible to observe an offset in the lift coefficients (Figure 1a) up to α = 14°. At this point, the lower Reynolds number arc suddenly produces more lift, and its trend merges with that of the arc at a Reynolds number of 218,000, which is known to have undergone transition [36]. At the exact same angle of attack, an abrupt reduction in drag can be noticed (Figure 1b). Furthermore, this coincides with a sudden downstream shift in the location of the trailing edge separation point (Figure 1c), in line with that of the arc experiencing turbulent flow.

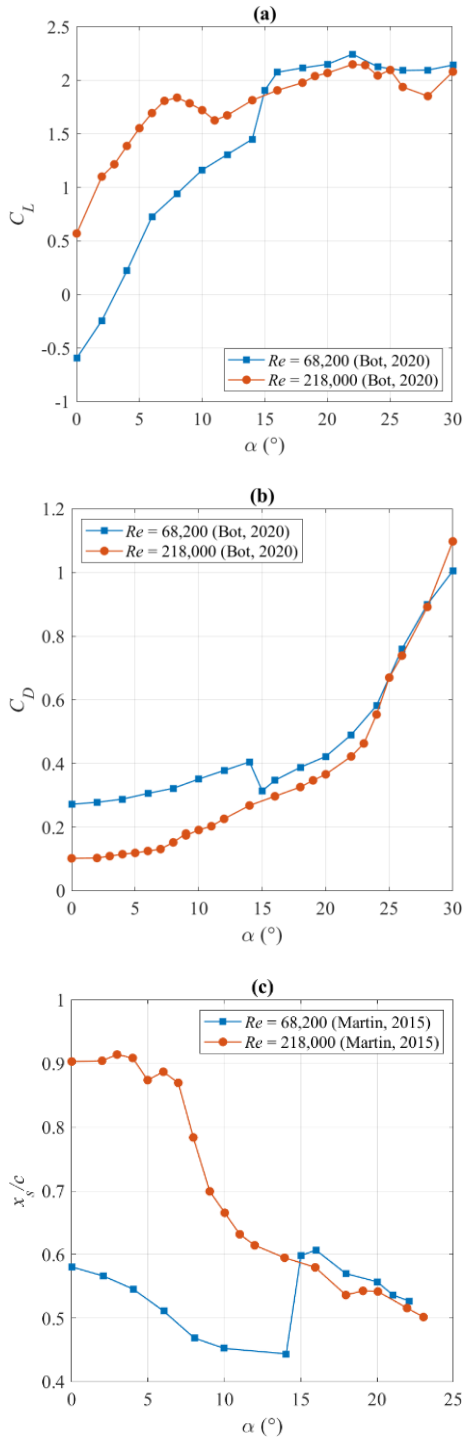

Figure 1. Lift (a) and drag (b) coefficients [13] and location of the trailing-edge separation point [34] (c) at a Reynolds numbers of 68,200 and 218,000.

These observations would indicate that the abrupt change in behaviour is the result of laminar-to-turbulent transition, occurring due to a critical angle of attack being reached at this particular value of the Reynolds number. This implies that a combination of a critical Reynolds number and a critical angle of attack are required to trigger transition, thus suggesting that, even following a leading-edge separation bubble, there can be a laminar boundary layer leading to laminar separation. Hence, this paper endeavours to assess the role of the leading-edge flow on boundary layer regime and turbulent separation, as well as the correlation between flow fields and global forces.

4. EXPERIMENTAL SETUP

4.1. Geometry

The geometry of the highly cambered, thin circular arc with a sharp leading edge under study is the same as that of Bot [13], with y_c/c = 22.32%, over chord lengths of 100 mm, 150 mm and 200 mm for the three arcs manufactured. The requirement for multiple chord lengths arose from the necessity to achieve a wider range of Reynolds number within the given flow speeds that could be achieved in the experimental facilities.

Carbon fibre prepreg was employed to achieve the required strength and stiffness at the lowest possible thickness, namely 1.8 mm. This is primarily motivated by the will to achieve as thin as possible a wing, as per yacht sails, but also prevent any upstream pressure increase and associated alteration in effective angle of attack that can arise from a thicker section. The relevant specifications are presented in Table 1, and a representative geometry is depicted in Figure 2.

Table 1. Geometric definition of the circular arcs employed.

Circular Arc	100 mm Arc	150 mm Arc	200 mm Arc
Chord, c (mm)	100	150	200
Span, s (mm)	370	370	370
Camber, y_c (mm)	22.32	33.48	44.64
Camber-to-chord ratio, y_c/c	22.32%	22.32%	22.32%
Chordwise draft location to chord ratio, f/c	50%	50%	50%
Leading edge and trailing edge angles (°)	48	48	48
Thickness, t (mm)	1.80	1.80	1.80

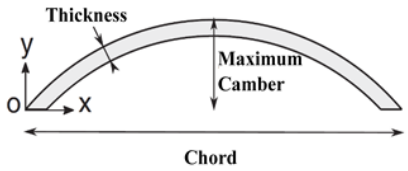

Figure 2. Experimental geometry, adapted from [13].

4.2. Towing tank testing

Part of the force measurements were undertaken in a towing tank, having a length of 60 m, breadth of 3.7 m, depth of 1.8 m and top speed of 4.6 m.s^{-1} [39]. The circular arc was fitted between end plates to achieve a 2D section. The lift and drag were recorded at 1000 Hz for six seconds once the desired speed was reached. Forces created by the test rig including end plates were subtracted, and resulting forces from the circular arc section were converted into force coefficients for lift and drag.

Considering the fluid's density ρ, the surface area given as the product of the span s and chord c, and the free stream velocity U_∞, the lift L and drag D yield the associated coefficients C_L and C_D, using Eq. 1 and Eq. 2 respectively:

$$C_L = \frac{L}{\frac{1}{2}\rho c s U_\infty^2}, \quad (1)$$

$$C_D = \frac{D}{\frac{1}{2}\rho c s U_\infty^2}. \quad (2)$$

4.3. Water tunnel testing

The water tunnel at the University of Edinburgh provided flow visualisation, as well as the ability to conduct additional force measurements. The 12 m long water tunnel features a breadth of 0.4 m, a depth of 0.9 m [39] with a water level at 0.34 m in this instance, and an ideal operating speed range between 0.15 m.s^{-1} (below which high turbulence intensity can interfere with the measurements) and 0.4 m.s^{-1} (after which wave interference begins). Force measurements were realised by employing a six-axis force/torque sensor, allowing for forces to be recorded up to ±35 N for the lift, and ±25 N for the drag, with a resolution of 1/160 N [40]. Moments could be quantified up to ±250 N.mm around all three axis; this proved a limiting factor on the 200 mm chord length geometry at higher flow speeds, thus further justifying the need for varying arc sizes. The data was sampled at 1000 Hz for 45 seconds. This is substantially longer than the record time in the towing tank, owing to both the limited run length and therefore run time in the towing tank, but also the higher expected streamwise turbulence intensity in the water tunnel, measured using laser doppler velocimetry as 3.63%.

4.4. Particle image velocimetry

A 200 mJ Nd:YAG pulsed laser at a wave length of 532 nm was employed to illuminate silver coated hollow glass spheres, with a nominal 14 µm diameter and specific gravity of 1.7, and images having a 2056 px by 2060 px resolution. The laser sheet, of thickness lesser than 2 mm, was directed parallel to the onset flow, illuminating the upper surface of the arc at midspan. The work of Bot et al. [36] having previously characterised the flow field around both the pressure and suction side of the same geometry, it is expected only the flow around the suction side will be of interest for the speeds and angles of attack investigated, hence no flow visualisation of the underside of the arc was undertaken. Indeed, it is the LESB, boundary layer and trailing-edge separation on the suction side that are of primary relevance in the present research.

Each particle image velocimetry flow visualisation featured a minimum of 100 pairs of images sampled at 7.5 Hz. A multi-pass (decreasing size) cross-correlation was adopted, with two initial passes having a 96 px by 96 px interrogation window and 50% overlap, before a final 32 px by 32 px pass with a 75% overlap.

5. VALIDATION AND EQUIVALENCE OF EXPERIMENTAL SETUP

5.1. Flow Bidimensionality

Firstly, the effectiveness of the end plates was ascertained, a vital process considering the low aspect ratio (AR) of the 200 mm chord test geometry ($AR = s/c = 1.85$). Lift and drag where recorded in the towing tank, for angles of attack ranging from 10° to 25° in one degree increment at Re = 53,530. The results were evaluated against the wind tunnel tests of Velychko [27], with an identical cross section, but an aspect ratio of 10. The comparison is shown in Figure 3.

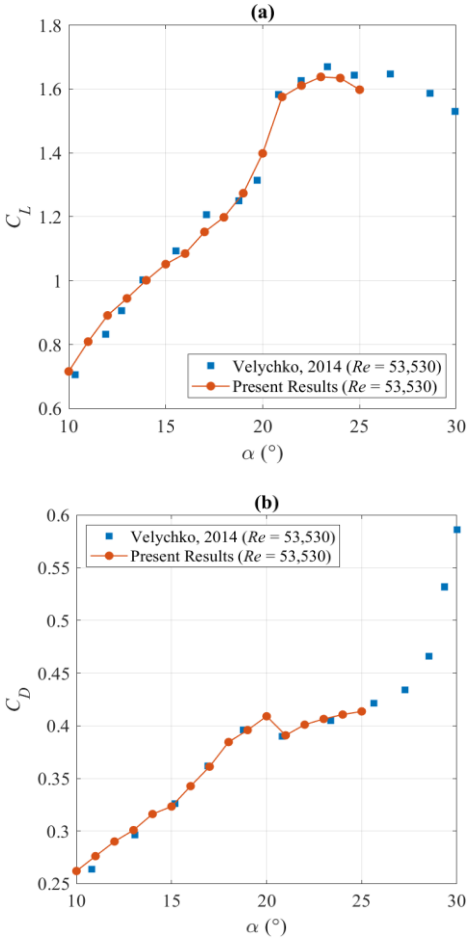

Figure 3. Lift (a) and drag (b) coefficients comparison between wind tunnel [27] (AR = 10) and towing tank (AR = 1.8) on identical circular arcs (y_c/c = 22.32%), both fitted end plates, at Re = 53,530.

Due to the difference in achievable flow velocities between the towing tank and water tunnel, different chord lengths had to be used to achieve the same Reynolds number range, as well as widen it. In order to guarantee the reliability of testing different chord length geometries, a repeatability experiment at Re = 68,200 was conducted, with arcs of 100 mm and 150 mm chord length respectively. The lift and drag coefficients are presented in Figure 4.

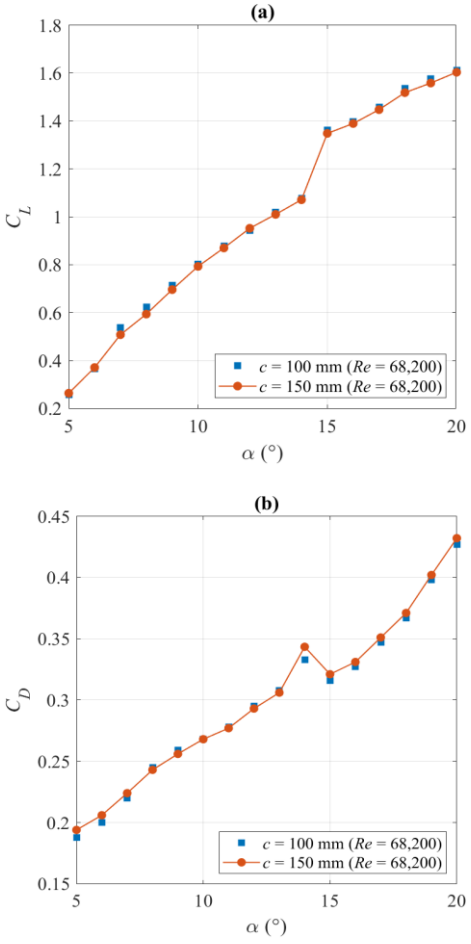

Figure 4. Lift (a) and drag (b) coefficients for arcs of 100 mm and 150 mm chord length respectively, at Re = 68,200.

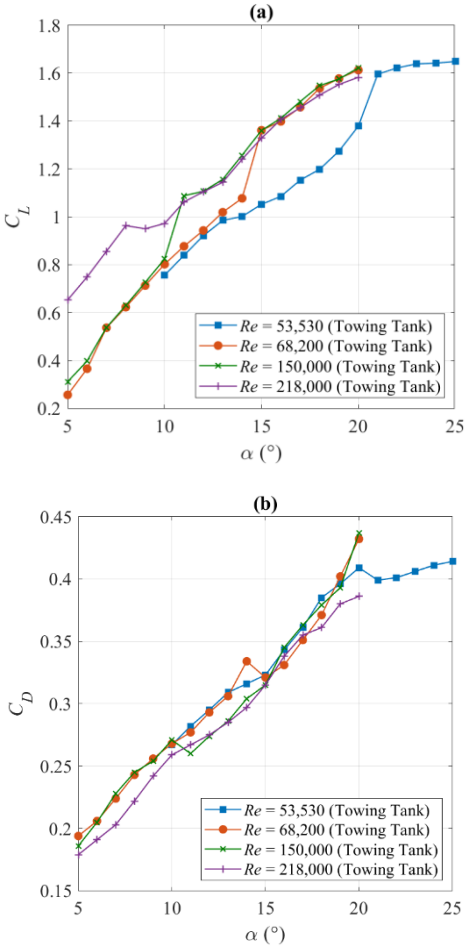

Figure 5. Lift (a) and drag (b) coefficients recorded in the towing tank, at Re = 68,200.

5.2. Towing tank force measurements

Towing tank tests were performed at Reynolds numbers comparable to that of the literature, namely 53,530 [27], 68,200 [32, 34], 150,000 (arbitrarily chosen to provide intermediate data) and 218,000 [32, 34]. The angles of attack ranged from 5° to 25°. The results are depicted in Figure 5.

For increasing Reynolds number, a shallower critical angle of attack is needed for transition to occur and thus induce a sharp lift increment. It also appears that a Reynolds-number-independent pre-critical trend exists. In the case of Re = 218,000, the increase in lift coefficient occurs at zero degrees angle of attack, an effect known as the lift crisis [36]. Moreover, in the post-critical range, a common trend is also present. These observations are in favour of the hypothesis that the abrupt change in lift and drag coefficient is due to laminar-to-turbulent transition.

6. RESULTS

6.1. Ideal angle of attack and associated critical Reynolds number

The ideal angle of attack, defined as the angle of incidence when the stagnation point is on the leading edge, was previously suggested at a value of either 8° [34] or 9° [31], likely under the misconceived assumption that the idea angle of attack can be identified by a local maximum in the lift, and without supporting flow visualisation evidence of a leading-edge separation bubble until α = 12° [35], though the ideal angle of attack may depend on Re [13]. The present study employed particle image velocimetry to locate the stagnation point on the arc, starting at the lowest suggested value of α = 8°, and increasing until the ideal angle of attack was reached, and then exceeded. Thus, the flow field and its relation to the lift coefficient's trend at the idea angle of attack can be characterised. Knowledge of the ideal angle of attack is important in the case of a soft membrane, as it constitutes the minimum angle of attack required for inflation. In the case of downwind yacht sails, a lower angle of incidence would not inflate the sail, thus rendering it unusable. As illustrated in Figure 6, the ideal angle of attack was ascertained to be 11°.

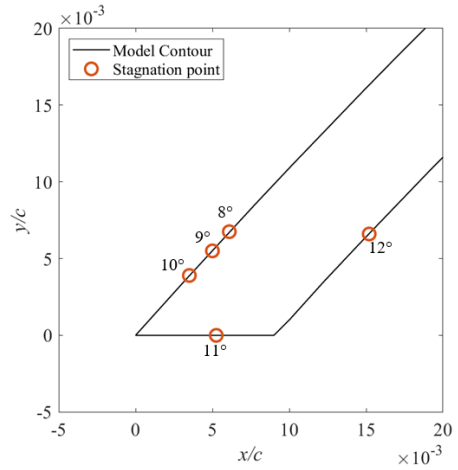

Figure 6. Location of the stagnation point near the leading edge for different angles of attack at Re = 68,200.

The circular arc was then tested at increasing flow speeds to determine the critical Reynolds number at α = 11°, for y_c/c = 22.32% at Re = 68,200. Results for lift and drag coefficients, presented in Figure 7, clearly show the change in behaviour at Re = 144,000 (+/- 2,000). This particular Reynolds number, i.e. the critical Reynolds number at the ideal angle of attack (for y_c/c = 22.32% at Re = 68,200), therefore represents the minimum required value during model scale testing of downwind sails to ensure a turbulent flow, representative of full-scale behaviour, is replicated.

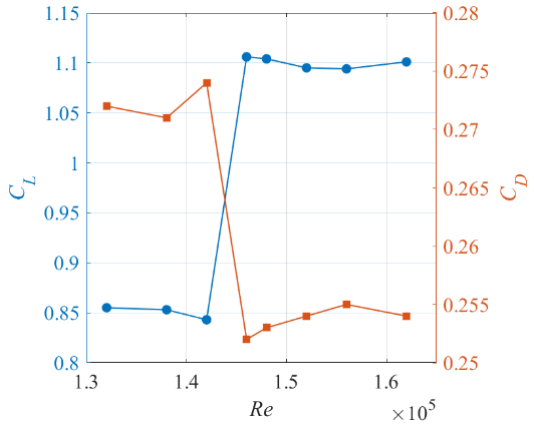

Figure 7. Lift and drag coefficient for increasing Reynolds number at the ideal angle of attack.

6.2. Separation point

The behaviour of the force coefficients, namely an increase in lift with an associated drop in drag, is consistent with the laminar-to-turbulent transition. This is further strengthened by the downstream shift in the separation point observed in the time-averaged PIV flow fields. Indeed, separation occurs further upstream prior to the critical angle of attack, and reaches a similar location as that of a higher Reynolds number, where the flow is turbulent, when surpassing the critical angle of attack. The location of the separation point over a range of pre and post-critical incidences can be found in Figure 8, yielding a similar behaviour as found in the literature [34].

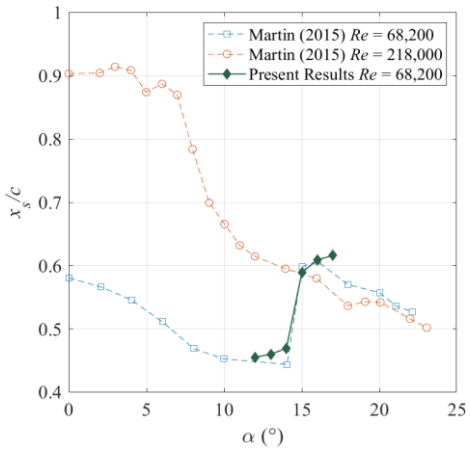

Figure 8. Streamwise location of the separation point at Re = 68,200 and comparison with Martin [34].

6.3. Turbulent kinetic energy at Re = 68,200

To further describe the flow field and the role of the leading-edge flow on trailing-edge separation as well as boundary layer regime, the nondimensional turbulent kinetic energy (TKE), κ, given by Eq. 3, was calculated.

$$\kappa = \frac{\overline{(u')^2} + \overline{(v')^2}}{2U_\infty^2} \qquad (3)$$

This is a function of the streamwise and streamnormal velocity fluctuations u' and v', and free stream velocity U_∞. TKE is commonly employed to characterise turbulent flow on flat plates [41], thick airfoils [42, 43, 44], low camber membranes [45, 46], as well as high camber wings [47, 48, 49]. The literature further reveals comparable magnitudes of κ on cambered profiles (*e.g.* $0 < \kappa < 0.2$ [43]). Visual representations, plotted in relation to the separation point, can be found in Figure 9, with the threshold to plot TKE defined as 0.01 [43, 45].

A clear distinction can be made between the sub-critical range, namely angles of attack of 12°, 13° and 14°, where moderate values of κ are exhibited, at a clear distance downstream of separation and away from the surface of the arc. Conversely, in super-critical territory, above α = 15°, higher values of κ are found, and detected upstream of the separation point. It is therefore possible to conclude that laminar separation occurs in one case, whereas the separation is turbulent in the other, explaining the increase in lift, reduction in drag, and delayed separation previously noticed. Note that past the critical angle of attack, the fluctuations appear to weaken and move away from the surface as the incidence increases, as observed on membrane airfoils [45].

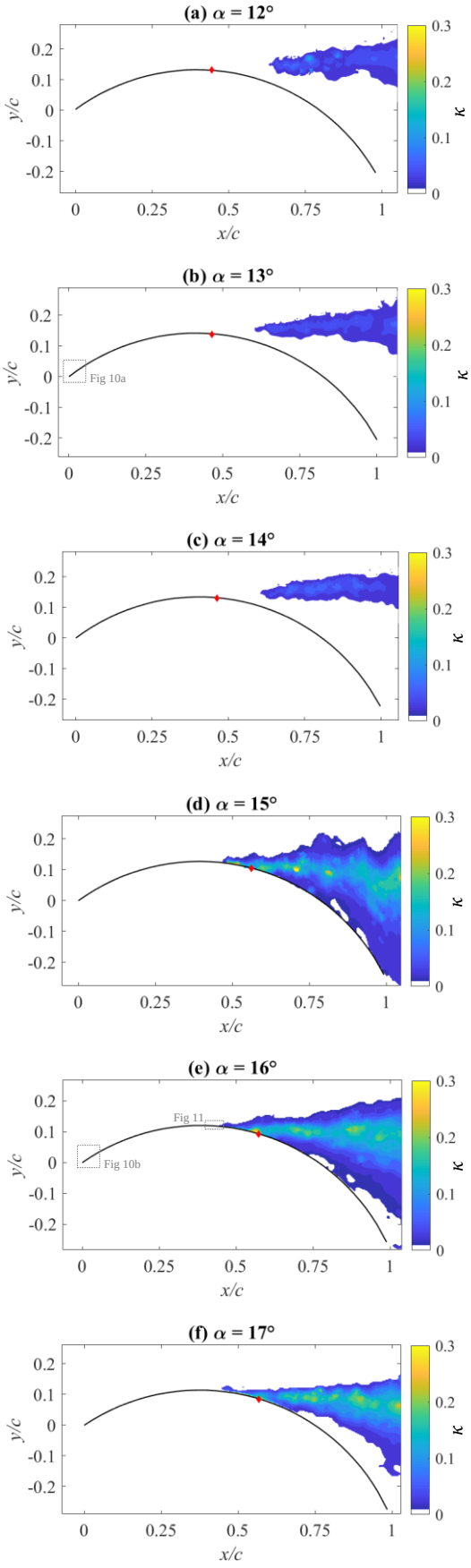

Figure 9. Nondimensional turbulent kinetic energy κ (plotted for κ > 0.01) and location of the separation point (♦) at Re = 68,200 over a range of pre (a-c) and post (d-f) critical angles of attack.

By capturing the overall flow field around the entirety of the arc, resolution is sacrificed, therefore not allowing to characterise the flow regime within the boundary layer, or at the leading edge, the latter being of particular interest on such geometries [39]. Thus, further investigation focussed on the LESB resulting from the leading-edge separation occurring past the ideal angle of attack was conducted.

6.4. Leading-edge separation bubble at Re = 68,200

A similar methodology was applied at the leading edge to quantify the TKE in both pre and post-critical regimes, at α = 13° and α = 16° respectively, for a Reynolds number of 68,200. Prior to reaching the critical angle of attack, a turbulent LESB is evident in Figure 10a. Remarkably, it is followed not by a turbulent boundary layer as might be expected, but by a laminar one, ascertained due to the absence of turbulent kinetic energy. On the other hand, at α = 16°, i.e. once the critical angle of attack has been exceeded, higher values of κ have been quantified, extending past the LESB into a turbulent boundary layer, as depicted in Figure 10b. In both cases, there is no significant difference in LESB size, or contribution to the overall lift, as later shown in section 6.5.

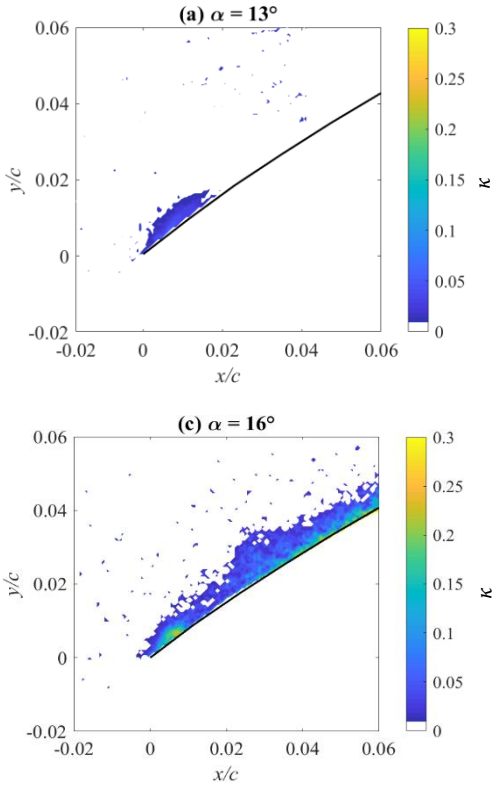

Figure 10. Nondimensional turbulent kinetic energy κ (plotted for κ > 0.01) at the leading edge pre (α = 13°) and post (α = 16°) critical angle of attack at Re = 68,200.

The nondimensional turbulent kinetic energy therefore appears to be constrained to the leading-edge separation bubble in sub-critical regime, and is followed by a laminar boundary layer. Conversely, the TKE carries on past the leading-edge separation bubble into the boundary layer when the critical angle of attack is exceeded.

In Section 6.3, the overall flow field across the whole geometry presented in Figure 9 highlighted the turbulent separation in post-critical regime, with turbulent kinetic energy visible ahead of the separation point. However, at that scale, the flow within the boundary layer was not captured. The focus on the leading edge in Figure 10 revealed that a turbulent boundary layer was indeed present past the LESB at α = 16°. Additional PIV downstream of the leading edge but upstream of the point where turbulent kinetic energy was detected in Figure 9e yielded the results for κ presented in Figure 11.

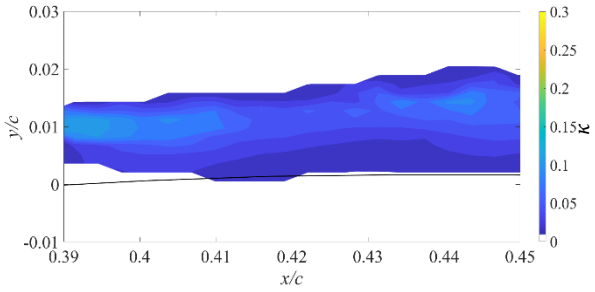

Figure 11. Nondimensional turbulent kinetic energy κ (for κ > 0.01) at α = 16° and Re = 68,200.

This evidence of a turbulent boundary layer between the two previously observed regions suggests that the turbulent boundary layer that follows the LESB in post-critical condition is carried along the surface of the arc all the way to the downstream trailing-edge separation.

6.5. Leading-edge separation bubble at Re = 53,530

The size of a leading-edge separation bubble increases with the angle of incidence and reduced flow speed. A case at these extremes of the presented set of experiments was therefore selected, while being in the turbulent regime. Figure 12 presents the LESB at α = 25° and Re = 53,530. In this condition, levels of κ consistent with previous measurements are exhibited in Figure 12a, while a primary recirculation bubble is also present in Figure 12b. However, contrarily to the work undertaken on flat plates [50] or some work on circular arcs [51] no secondary bubble could be observed at the available PIV resolution. Nevertheless, it could be speculated that the upstream inflection in the mean streamwise velocity contour (u/U_∞ = 0) [50] in Figure 12b may be the result of such a secondary bubble.

From the three cases focussed on the leading edge, as presented in Figures 10a, 10b and 12, the circulation Γ can be quantified as the integral of vorticity over the leading-edge separation bubble area. As the LESB does not move with respect to the arc, its circulation is part of the bounded circulation of the arc and its lift contribution can be computed with the Kutta-Joukowski lift formula:

$$L = \rho U_\infty \Gamma \qquad (4)$$

Whether in pre or post-critical regime, for a similar size leading-edge separation bubble, as shown for Re = 68,200 at α = 13° and α = 16°, comparable contributions to the overall lift of the circular arc are made, namely circa 2%. Conversely, for the larger LESB at Re = 53,530 and α = 25°, the contribution to overall lift rose to 7.5%.

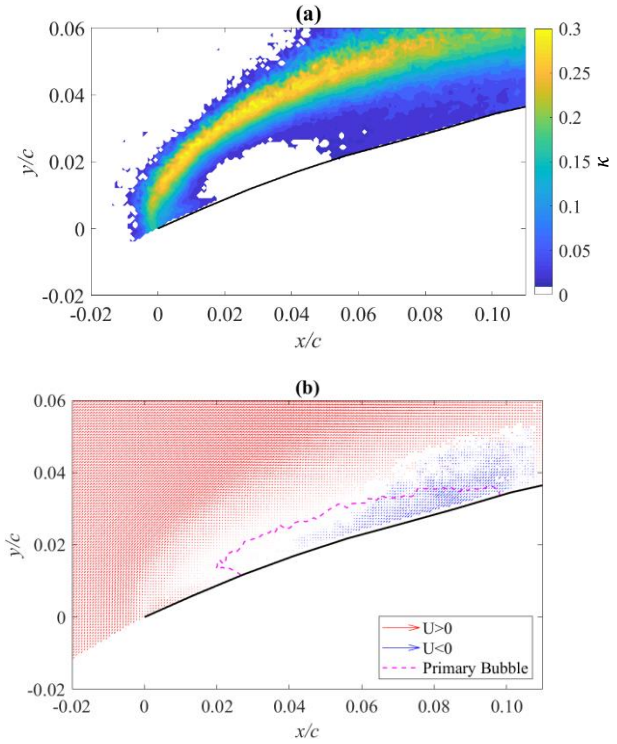

Figure 12. Leading-edge separation bubble at α = 25° and Re = 53,530, depicting (a) nondimensional turbulent kinetic energy κ (for κ > 0.01), and (b) velocity field with streamwise (red) and backwards (blue) flow.

It can therefore be concluded that the LESB provides a non-negligible contribution to the overall lift, and a larger LESB induces a greater contribution to lift. This is not to say that the lift is enhanced by the presence of the LESB [52], but rather that part of the lift is provided by the LESB. Furthermore, these findings reveal the critical effect of the LESB on the boundary layer regime and overall flow fields, ultimately affecting the global forces.

7. DISCUSSION

Based on the presented experimental data and literature [13, 27], Figure 13 proposes a schematic description of the lift trend with the angle of attack and the Reynolds number. This is presented without values for the lift coefficient as the onus is on its behaviour, with the actual values, which may be impacted by various factors such as blockage, not deemed relevant for this representation.

Two main trends can be distinguished, namely a laminar and turbulent one, with an abrupt transition occurring when the critical angle of attack is reached. The general behaviour of the turbulent trend for the tested arc length and leading edge shape, increasing the angle of attack from zero, can be characterised as follows:

- There is a first angle of attack range ($0° < \alpha < 8°$) where the lift increases almost linearly with a slope higher than 2π/radians.

- Trailing-edge separation becomes significant as the separation point moves upstream, resulting in a reduced lift trend with incidence ($8° < \alpha < 11°$).

- Ideal angle of attack ($\alpha = 11°$) is reached, where the upstream stagnation point is at the leading edge.

- Subsequently, the leading-edge separation bubble grows in size with the angle of attack ($11° < \alpha < \sim 23°$), associated with an increase in lift.

- Deep stall is eventually reached ($\alpha \gtrsim 23°$), with the flow separating at the leading edge and no longer reattaching to the surface of the arc, with a noticeable drop in lift being generated [13].

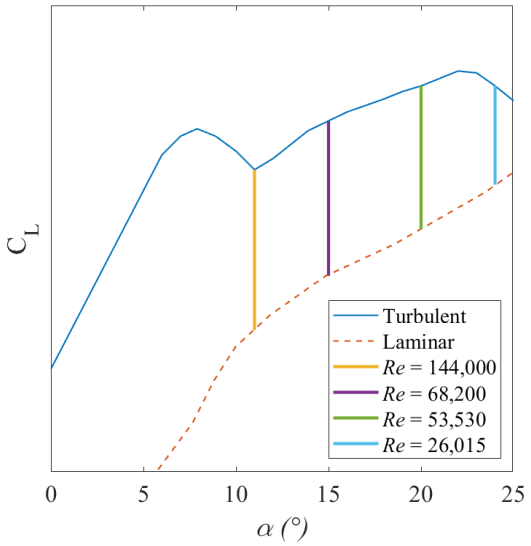

Figure 13. Idealized model for the lift generated by a highly cambered thin circular arc with sharp leading edge, including data edited from Velychko [27] and Bot [13].

With the acquired knowledge of the ideal angle of attack (11° for y_c/c = 22.32% at Re = 68,200) and corresponding critical Reynolds (144,000 +/-2,000), it is possible to recommend experimental model testing conditions so that the full-scale flow, clearly turbulent, can be replicated in a wind tunnel for instance. Indeed, as highlighted by Souppez et al. [37], evidence of laminar separation bubbles, identified thanks to a characteristic plateau in the pressure distribution, can be found in the literature, revealing inappropriate test conditions. Furthermore, the interesting case of Bot et al. [53] provides a striking example of a rigid model scale test undertaken at too low a Reynolds number in certain conditions. Indeed, pressure distribution at the shallowest incidence reveals the presence of a laminar separation bubble, suggesting the critical angle of attack has not yet been reached. However, at all subsequent and greater incidences, such flow feature is absent, and thus the critical angle of attack to trigger transition must have been reached. Given the typical Reynolds number of full scale spinnakers being of the order of 5×10^5 to 5×10^7 [39], the present findings are relevant to model scale testing.

Most remarkably, the nondimensional turbulent kinetic energy evidences the fact that, in pre-critical regime, where the downstream separation is laminar, the LESB is turbulent, but followed by a laminar boundary layer all the way to the training edge separation, before transition occurs in the wake. Conversely, in post-critical regime, the turbulent LESB is followed by a turbulent boundary layer, which is carried all the way to separation. Lastly, it was shown that, for a given leading-edge separation bubble size, the flow regime immediately downstream of the LESB does not make a significant difference to the lift contribution at the leading edge. However, a larger LESB proved to contribute to the overall lift by a greater proportion. Furthermore, it is the overall flow regime, whether laminar or turbulent, initiated at the inception of the boundary layer, that influences the global forces.

8. CONCLUSIONS

By employing a combination of force measurements and PIV flow visualisation, this study provides new insights on the flow around a circular arcs, particularly on the crucial effect of the leading-edge flow on the trailing-edge separation. More precisely, this was applied to a highly cambered (y_c/c = 22.32%), thin circular arc, with a sharp leading edge.

Evidence of a combination of critical Reynolds number and critical angle of attack necessary to trigger laminar-to-turbulent transition has been provided, with the sudden change in flow regime accounting for the sharp increase in lift and drop in drag. Additionally, the ideal angle of attack, where the stagnation point is located on the sharp leading edge has been identified, confirming previous observation of the formation of a leading-edge separation bubble once this incidence is exceeded.

Most importantly, the present research study shed a new light on the effect of the leading-edge separation bubble on the flow within the downstream boundary layer. Indeed, below the critical angle of attack, while a turbulent leading-edge separation bubble was present, the boundary layer remained laminar all the way to the trailing edge separation, with transition occurring in the detached wake. On the other hand, once the critical angle of attack is surpassed, the turbulent leading-edge separation bubble is followed by a turbulent boundary layer along the surface of the arc until turbulent separation occurs.

It is envisaged that these results will contribute to improve the design and performance of high-performance downwind yacht sails, and may further contribute to wider industrial applications, including micro aerial vehicles.

References

1. Fallow, B. J., (1996), “America's Cup sail design”, *Journal of Wind Engineering and Industrial Aerodynamics*, **63**, 183-192.
2. Richards, P. J., Johnson, A. & Stanton A., (2001), “America’s Cup sails – vertical wings or horizontal parachutes?”, *Journal of Wind Engineering and Industrial Aerodynamics*, **89**, 1565-1577.
3. Viola, I. M. & Flay, R. G. J. (2009), “Force and pressure investigation of modern asymmetric spinnakers”, *International Journal of Small Craft Technology*, **151**(B2).
4. Flay, R. G. J. & Jackson, P. S. (1992), “Flow simulation for wind tunnel Studies of sail aerodynamics”, *Journal of Wind Engineering and Industrial Aerodynamics*, **41**, 2703-2714.
5. Flay, R. G. J. & Vuletich, I. J., (1995), “Development of a wind tunnel test facility for yacht aerodynamic studies”, *Journal of Wind Engineering and Industrial Aerodynamics*, **58**, 231-258.
6. Hedges, K. L., (1993), *Computer modelling of downwind sails,* ME Thesis, University of Auckland, New Zealand.
7. Lasher, W. C., Sonnenmeier, J. R., Forsman, D. R. & Tomcho, J., (2005), “The aerodynamics of symmetric spinnakers”, *Journal of Wind Engineering and Industrial Aerodynamics*, **93**, 311-337.
8. Hedges, K., Richards, P. & Mallison, G., (1996), “Computer modelling of downwind sails”, *Journal of Wind Engineering and Industrial Aerodynamics*, **63**, 95-110.
9. Milgram, J. H., (1968), “The Aerodynamic of sails”, *Proceedings of the 7th Symposium on Naval Hydrodynamic*, 1397-1434.
10. Gentry, A., (1971), *“The aerodynamics of sail interaction”, The Ancient Interface III, 3rd AIAA Symposium on Sailing*, California, US.
11. Gentry, A., (1988), “The application of computational fluid dynamics to sails”, *Proceedings of the Symposium of Hydrodynamic Performance Enhancement for Marine Applications.*
12. Flay, R. G. J., Piard, A. & Bot, P., (2017), “Aerodynamics of a highly cambered circular arc aerofoil: experimental investigations”, *International Conference on Innovation in High Performance Sailing Yachts*, Lorient, France, 150-162.
13. Bot, P., (2020), “Force variation related to flow pattern changes around a high-camber thin wing”, *AIAA Journal*, 1-7.
14. Souppez, J.-B. R. G., Arredondo-Galeana, A. & Viola, I. M., (2019), “Recent advances in numerical and experimental downwind sail aerodynamics”, *Journal of Sailing Technology*, **4**(1), 45-65.
15. Wallis, R. A., (1946), *Wind tunnel tests on a series of circular arc plate aerofoils*, Melbourne: Aeronautical Research Labs.
16. Maekawa, T. & Atsumi, S., (1952), *Transition caused by the laminar flow separation,* Washington, National Advisory Committee for Aeronautics, Technical Memorandum 1352.
17. Tani, I., (1940), “On the transition caused by laminar separation of the boundary layer”, *Jour. Soc. Aero. Sci. Japan,* **7**.
18. Owen, P. R. & Klanfer, L., (1955), *On the laminar boundary layer separation from the leading edge of a thin airfoil,* Ministry of Supply, Aeronautical Research Council.
19. DeLaurier, J. D. & Harris, J. M., (1974), “An experimental investigation of the aerodynamic characteristics of stepped-wedge airfoils at low speeds”, *Second International Symposium on the Technology and Science of Low-Speed and Motorless Flight*, Massachusetts, US.
20. Buehring, I., (1977), *Performance characteristics of simple airfoils for windmill applications*, London, Imperial College.
21. Bruining, A., (1979), *Aerodynamic characteristics of a curved plate airfoil section at reynolds numbers 60.000 and 100.000 and angles of attack from -10 to +90 degrees*, Delft: Delft University of Technology, Department of Aerospace Engineering.
22. Pandey, M., Pandey, K. P. & Ojha, T. P., (1988). “Aerodynamic characteristics of cambered steel plates in relation to their use in wind energy conversion systems”, *Wind Engineering,* **12**(2), 90-104.
23. Tse, M. C., (1991), *Overall effects of separation on thin aerofoils,* PhD Thesis, McGill University, Canada.
24. Cyr, S., (1992), *A theoretical model for flow about a circular-arc aerofoil with separation*, MSc Thesis, McGill University, Canada.
25. Sunada, S., Yasuda, T., Yasuda, K. & Kawachu, K., (2002), “Comparison of wing characteristics and an ultralow Reynolds number”. *Journal of Aircraft,* **39**.
26. Okamoto, M. & Azuma, A., (2005), “Experimental study on aerodynamic characteristics of unsteady wings at low Reynolds number”, *AIAA Journal,* **42**(12), 2526-2536.
27. Velychko, N., (2014), *Study of highly cambered aerofoil using JR3 sensor.* Aerodynamics laboratory report, The University of Auckland, New Zealand.

28. Brault, E., (2013), *Aerodynamics on very thin airfoil,* MSc Thesis, Newcastle University.
29. Milgram, J. H., (1971), *Section data for thin, highly cambered airfoils in incompressible flow*, NASA CR-1767, United States.
30. Cyr, S. & Newman, B. G., (1996), "Flow past two-dimension membrane aerofoils with rear separation", *Journal of Wind Engineering and Industrial Aerodynamics,* **63**, 1-16.
31. Collie, S. J., Kackson, P. & Fallow, B. J., (2004), "Two-dimensional CFD-based parametric analysis of downwind sail designs", *International Journal of Small Craft Technology,* **146**:15.
32. Lombardi, A., (2014), *Experimental analysis of highly-cambered thin profile,* MSc Thesis, IRENAV, France.
33. Lebret, C., (2013), *High cambered thin profile study,* Internship report, IRENAV, France.
34. Martin, V., (2015), *Reynolds number and angle of attack effects on a highly cambered thin profile flow topology,* MSc Thesis, IRENAV, France.
35. Thomas, G., (2015), *Flow phenomenology around a highly cambered thin profile*, MSc Thesis, IRENAV, France.
36. Bot, P., Rabaud, M., Thomas, G., Lombardi, A. & Lebret, C., (2016), "Sharp transition in the lift force of a fluid flowing past nonsymmetrical obstacles: evidence for a lift crisis in the drag crises regime", *Physical review letters,* **117**.
37. Souppez, J.-B. R. G., Arredondo-Galeana, A. & Viola, I. M., (2019), "Recent advances in downwind sail aerodynamics", *Proceedings of the 23rd Chesapeake Sailing Yacht Symposium*, Annapolis, Maryland, United States, March 2019.
38. Dewavrin, J. M. M.-A. & Souppez, J.-B. R. G., (2018), "Experimental investigation into modern hydrofoils-assisted monohulls: how hydrodynamically efficient are they?", *International Journal of Small Craft Technology,* **160**(2), 111-120.
39. Arredondo-Galeana, A. & Viola, I. M., (2017), "The leading-edge vortex of yacht sails", *Ocean Engineering,* **159**, 552-562.
40. Bird, H. J. A., Otomo, S., Ramesh, K. & Viola, I. M., (2019), "A geometrically non-linear time-domain unsteady lifting-line theory", *AIAA SciTech Forum*, California, United States.
41. Lee, D., Kawau, S., Nonomura, T., Anyoji, M., Aono, H., Oyama, A., Asai, K. & Fujia, K. (2015), "Mechanisms of surface pressure distribution within a laminar separation bubble at different Reynolds numbers", *Physics of Fluids,* **24**, 85-105.
42. Choudhry, A., Arjomandi, M. & Kelso, R., (2015), "A study of long separation bubble on thick airfoils and its consequent effects", *International Journal of Heat and Fluid Flows,* **52**, 84-96.
43. Koca, K., Genc, M. S., Acikel, H. H., Cagdas, M. & Bodur, T. M., (2018), "Identification of flow phenomena over NACA4412 wind turbine airfoil at low Reynolds numbers and role of laminar separation bubble on flow evolution", *Energy,* 750-764.
44. Istvan, M. & Yarusevych, S., (2018), "Effect of free-stream turbulence intensity on transition in a laminar separation bubble formed over an airfoil", *Experiments in Fluids,* **59**.
45. Rojratsirikul, P., Wang, Z. & Gursul, I., (2009), "Unsteady fluid-structure interactions of membrane airfoils at low Reynolds numbers", *Experiments in Fluids,* **46**, 859-872.
46. Rojratsirikul, P., Genc, M. S., Wang, Z. & Gursul, I., (2011), "Flow-induced vibrations of low aspect ratio rectangular membrane wings", *Journal of Fluids and Structures,* **27**, 1296-1309.
47. Nava, S., Carter, J. E. & Norris, S. E., (2018), "Large eddy simulation of an asymmetric spinnaker", *Ocean Engineering,* **169**, 99-109.
48. Nava, S., Bot, P., Cater, J., Norris, S., (2016), *"Modelling the Lift Crisis of a Cambered Plate at 0° Angle of Attack"*, 20th Australasian Fluid Mechanics Conference, Perth, Australia, December 2016.
49. Souppez, J.-B. R. G. & Viola, I. M., (2020), "Aerodynamics of highly cambered circular arcs with a sharp leading edge at low Reynolds numbers", *Bulletin of the American Physical Society*, 73rd Annual Meeting of the APS Division of Fluid Dynamics, Chicago, United States, November 2020.
50. Crompton, M. & Barrett, R., (2000), "Investigation of the separation bubble formed behind the sharp leading edge of a flat plate at incidence", *Proceedings of the Institution of Mechanical Engineers, Part G,* **214**, 157-176.
51. Couvrant, H., (2015), *Reynolds number and angle of attack effects on a leading edge vortex for a high cambered thin profile,* MSc Thesis, IRENAV, France.
52. Arredondo-Galeana, A., (2019), *A study of the vortex flow of downwind sails,* PhD Thesis, The University of Edinburgh, United Kindgdom.
53. Bot, P., Viola, I. M., Flay, R. G. J. & Brett, J. S., (2014), "Wind-tunnel pressure measurements on model-scale rigid downwind sails", *Ocean Engineering,* **90**, 84-92.